RESEARCH ARTICLE

Key Points:
- The effect of surface water movement on methane emissions is incorporated into a methane model
- The effect of surface water transport on methane emissions varies in different regions
- Surface water plays an important role in determining inundation extent and methane emissions

Correspondence to:
X. Lu,
xlu@mbl.edu

A large-scale methane model by incorporating the surface water transport

Xiaoliang Lu[1,2], Qianlai Zhuang[3], Yaling Liu[4], Yuyu Zhou[5], and Amir Aghakouchak[6]

[1]Ecosystems Center, Marine Biological Laboratory, Woods Hole, Massachusetts, USA, [2]State Key Laboratory of Remote Sensing Science, Institute of Remote Sensing and Digital Earth, Chinese Academy of Sciences, Beijing, China, [3]Department of Earth, Atmospheric, and Planetary Sciences, Purdue University, West Lafayette, Indiana, USA, [4]Pacific Northwest National Laboratory, Joint Global Change Research Institute, College Park, Maryland, USA, [5]Department of Geological and Atmospheric Sciences, Iowa State University of Science and Technology, Ames, Iowa, USA, [6]Department of Civil and Environmental Engineering, University of California, Irvine, California, USA

Abstract The effect of surface water movement on methane emissions is not explicitly considered in most of the current methane models. In this study, a surface water routing was coupled into our previously developed large-scale methane model. The revised methane model was then used to simulate global methane emissions during 2006–2010. From our simulations, the global mean annual maximum inundation extent is 10.6 ± 1.9 km^2 and the methane emission is 297 ± 11 Tg C/yr in the study period. In comparison to the currently used TOPMODEL-based approach, we found that the incorporation of surface water routing leads to 24.7% increase in the annual maximum inundation extent and 30.8% increase in the methane emissions at the global scale for the study period, respectively. The effect of surface water transport on methane emissions varies in different regions: (1) the largest difference occurs in flat and moist regions, such as Eastern China; (2) high-latitude regions, hot spots in methane emissions, show a small increase in both inundation extent and methane emissions with the consideration of surface water movement; and (3) in arid regions, the new model yields significantly larger maximum flooded areas and a relatively small increase in the methane emissions. Although surface water is a small component in the terrestrial water balance, it plays an important role in determining inundation extent and methane emissions, especially in flat regions. This study indicates that future quantification of methane emissions shall consider the effects of surface water transport.

1. Introduction

Methane (CH$_4$), an important greenhouse gas, has about 22 times larger radiative forcing than CO$_2$. Wetlands play an important role in global methane budget contributing between 15 and 40% of the total source budget [*Denman et al.*, 2007]. Recent observations and modeling studies have shown that methane emission may act as a positive feedback to warming trend [*Eliseev et al.*, 2008; *Ringeval et al.*, 2011]. The future climate change is closely linked to methane emissions, and thus, quantification of methane emissions is critical in climate change assessment.

In recent 20 years, many progresses have been made in developing methane models which are particularly crucial in estimating how methane emissions respond to climate change. *Matthews and Fung* [1987] started the methane modeling by considering vegetation types, inundation maps, and the methane emission intensity. Afterward, more key controlling processes, such as methane production (methanogenesis), oxidation (methanotrophy), and transport have been linked to climate factors, vegetation types, soil texture, availability of carbon substrate, soil PH, and redox potential [*Walter and Heimann*, 2000; *van Bodegom et al.*, 2001; *Zhuang et al.*, 2006]. To estimate the methane emissions in high latitudes, the largest soil carbon pool, soil thermal modules were also incorporated to capture the impact of active layer depth on methane emissions [*Wania et al.*, 2009; *Zhuang et al.*, 2006]. Methane is generated under anaerobic conditions that occur in saturated lands and consumed under aerobic conditions that occur in unsaturated zone. Regional simulation of methane emissions requires accurate information on the area and period of inundation of land. The inundation extent, the most important factor in controlling methane release, is currently modeled in two ways: (1) prescribed or modulated by the static map-based inundation products [*Hodson et al.*, 2011; *Riley et al.*, 2011; *Ringeval et al.*, 2011, 2012; *Spahni et al.*, 2011; *Tian et al.*, 2011; *Wania et al.*, 2009, 2010], such as the Global Inundation Extent from Multi-Satellites (GIEMS) [*Prigent et al.*, 2007; *Papa et al.*, 2010] and the

Surface Water Microwave Product Series (SWAMPS) [*Schroeder et al.*, 2010] and (2) a time varying inundated area simulated from the hydrological modules contained in the methane frameworks [*Avis et al.*, 2011; *Hopcroft et al.*, 2011; *Singarayer et al.*, 2011].

The recent intercomparison of wetland methane emission models over West Siberia (WETCHIMP-WSL) [*Bohn et al.*, 2015] suggested that the models using inundation products may suffer from large biases in methane emissions, especially for those relying on the satellite inundation products alone. The reasons are (1) optical remote sensing lacks the ability to detect water surface under forest canopy or cloud cover, (2) infrequent temporal sampling of optical sensors, (3) remote sensing by radar may not retrieve large-scale water surface in a short time, and (4) low spatial resolution of microwave sensors [*Norouzi et al.*, 2015]. *Bohn et al.* [2007] suggested that uniform water table depth (WTD) directly derived from soil moisture content may lead to systematic biases. Therefore, the TOPMODEL-based formulation has been applied to redistribute simulated soil moisture in a coarser resolution to the finer resolution according to the local topographic information [*Lu and Zhuang*, 2012]. However, limitations of TOPMODEL in capturing lateral flow, distributed patterns of the water table, and inundation areas have been discussed in previous studies [e.g., *Blazkova et al.*, 2002; *Pike*, 1998]. Although many progresses have been achieved, the recent methane model intercomparison project on the global level (WETCHIMP) [*Melton et al.*, 2013; *Wania et al.*, 2013] suggested that lateral movement of water between gird cells, an important process describing contributions of upland water flow, was not explicitly considered in all the current methane models. The lack of this mechanism will underestimate both inundation extent and its duration.

On the basis of our previous effort which used the TOPMODEL approach to consider the effect of subgrid topography on methane emissions, a water surface routing model is incorporated in our large-scale methane model for the effect of surface water movement on inundation extent and methane emissions in this study. Using the new methane model, we then estimated the global methane dynamics from 2006 to 2010 and also analyzed how the surface water movement affects the inundation extent and methane emissions in different regions. In this study, we focus on methane emissions from natural ecosystems, while emissions from anthropogenic activities such as fossil fuels and biomass burning, landfills, rice cultivation, coal mining, and gas flare are not covered in this study.

2. Method

2.1. Overview of the Current Inundation and Methane Model

In our early studies, *Zhuang et al.* [2001, 2004, 2006] developed a methane model under the framework of the Terrestrial Ecosystem Model [*Melillo et al.*, 1993; *Zhuang et al.*, 2003] to simulate the methane emissions from northern high latitudes. Methane production is assumed to only occur in saturated zones and regulated by organic substrate availability, soil thermal conditions, soil PH, and soil redox potentials; methane oxidation occurs in unsaturated zone of soil and is a function of soil methane concentration, soil temperature, soil moisture, and soil redox potential. The three processes, diffusion, plant-aided transport, and ebullition, are considered in modeling methane transport. Water table depth that separates saturated and unsaturated zones in soil profile is calculated by a hydrological module and is assumed equally distributed in each simulation cell. This simple treatment of water table depth, however, neglects the effect of spatial heterogeneity on water table depth. *Lu and Zhuang* [2012] improved the original model in the three aspects: (1) a TOPMODEL-based approach [*Beven and Kirkby*, 1979] was developed to account for the effects of microtopography on the water table depth (WTD); (2) the Variable infiltration capacity (VIC) model [*Liang et al.*, 1994], a large-scale hydrology model, was used to simulate the hydrological processes and effects of freeze/thaw cycles on methane emissions dynamics; and (3) a function was built for the relationship between the methane emissions transport and soil temperature. The results showed that the methane model can capture the subgrid variations in the methane emissions and performs well under the complex freeze/thaw processes. The daily inundated area was described as

$$WTD_{VIC+Topmodel} = WTD_{VIC} - m \times (TWI - VIC_{TWI}) \tag{1}$$

$$
\begin{aligned}
I_{VIC+Topmodel} &= 0, \quad \text{if } WTD_{VIC+Topmodel} > 0 \\
I_{VIC+Topmodel} &= 1, \quad \text{if } WTD_{VIC+Topmodel} <= 0
\end{aligned}
\tag{2}
$$

where TWI is the local topographic wetness index [*Beven and Kirkby*, 1979] at the subgrid level (0.25° in this study) and VIC_{TWI} is mean topographic index for a specific VIC simulation grid cell (1° in this study). WTD_{VIC} is the water table depth derived from daily simulated soil moisture and porosity, and $WTD_{VIC+Topmodel}$ is the subgrid water table depth used in the methane simulation; m is the decay parameter, which describes the

change in soil conductivity with depth (meter, see Lu and Zhuang's paper [*Lu and Zhuang*, 2012] for its values). The inundation flag, $I_{VIC + Topmodel}$, is determined by subgrid water table depth $WTD_{VIC + Topmodel}$ at 0.25° spatial resolution (equation (2)): ground surface is inundated if water table depth is equal to or less than zero. The methane estimated from $I_{VIC + Topmodel}$ was shown that it can capture more heterogeneity effect [*Bohn et al.*, 2007; *Ringeval et al.*, 2012].

The current methane models considered two relevant factors in estimating inundation extent: (1) grid cell's water balance and (2) local topographic distribution. Both are independent from other neighbor simulation cells. The hydrological connection across grid cells, such as lateral water movement, is not considered in estimating inundation extent. Therefore, current methane models lack the ability to track lateral water movement and neglect its effect on methane emissions. Runoff moves from upland areas along with elevation gradient and eventually flows into rivers, which has a large contribution to inundation extent, especially in lowland areas. Previous studies have shown that water transport across grid cells can largely control the inundation extent in some large river basins [*Kim et al.*, 2009]. Since groundwater movement has very limited influence on generating inundated area, we focus on the surface water movement in this study.

2.2. The CaMa-Flood Model and Inundation Extent

To simulate surface water transport, a large-scale routing model is needed to track surface runoff estimated from a land surface process model on the ground surface and also in rivers. In this study, we used the Catchment-Based Macro-scale Floodplain (CaMa-Flood) [*Yamazaki et al.*, 2011, 2012a, 2012b] to route runoff generated by the VIC simulation and track its dynamics. The CaMa-Flood calculates water storage in river and floodplain reservoirs in each grid, and other variables, such as inundated area, river discharge, and water depth are derived from water storage. The CaMa-Flood model can be implemented at a different resolution from the VIC simulation. The simulated runoff from the VIC was assigned to each CaMa-Flood grid by the nearest neighbor interpolation. Although the CaMa-Flood model is usually applied at a relatively coarse resolution (0.25° in this study), the topographic information determining water transport is fully considered. For a specific 0.25° gird cell, the CaMa-Flood model provided the daily inundation extent which is denoted as $I_{VIC + CaMa - Flood}$. Note that $I_{VIC + CaMa - Flood}$ represents the flooded areas due to the contribution of surface runoff, and the inundation extent estimated from the TOPMODEL-based redistribution is still valid and may be overlapped with $I_{VIC + CaMa - Flood}$ in some regions. Therefore, the daily inundation extent (I_{new}) used in the methane model is estimated as

$$I_{new} = U\left[I_{VIC+Topmodel}，\ I_{VIC+CaMa-Flood} \right] \tag{3}$$

where U represents the union of $I_{VIC + Topmodel}$ and $I_{VIC + CaMa - Flood}$. From the equations (1) and (2), $I_{VIC + Topmodel}$ is a binary variable: either 1 (inundated) or 0 (not inundated); $I_{VIC + CaMa - Flood}$ and I_{new} can vary from 0.0 to 1.0, standing for the inundated fraction in each 0.25° grid. Soil column in inundated areas under surface water is assumed to be saturated due to water reinfiltration. Although we do not explicitly model the reinfiltration process, the water consumed in the reinfiltration should take only a small fraction of surface runoff and the daily time step should be enough for filling soil column. The lack of infiltration treatment will not change the surface inundation extent much and can significantly improve the efficiency of the simulation. See the supporting information for more explanation on the approaches estimating water table.

2.3. Incorporate I_{new} Into the Current Methane Module

In this study, soil moisture, soil temperature, and runoff were simulated at a 1° spatial resolution using the VIC model; runoff was simulated at a 0.25° spatial resolution using the CaMa-Flood model; and methane emission intensity was also calculated at the 0.25° spatial resolution (unit: g CH_4/m^2 d, Figure 1). Other input data sets for estimating methane emissions (such as NPP, PH, and soil texture) were also available at the 0.25° resolution. The soil temperature which is an output of the VIC simulation had a 1° resolution and was directly used in the methane module by the nearest neighbor interpolation (Figure 1).

If a 0.25° grid cell with the area of A (m^2) is completely inundated ($I_{new} = 1$) or noninundated ($I_{new} = 0$), the methane emissions (E, g CH_4/d) are calculated as $F1 * A$ and $F1$ is estimated from the methane model. However, I_{new} can vary from 0 to 1. It indicates that one 0.25° grid cell is partially inundated. In this case, methane may emit at two different intensities within a specific 0.25° grid cell. Although higher-resolution data ($I_{VIC + Topmodel} \approx I_{VIC + CaMa - Flood}$) are helpful to alleviate this problem, the computation load also increases at a square order. To reduce the computation time, we calculated two methane emission rates in
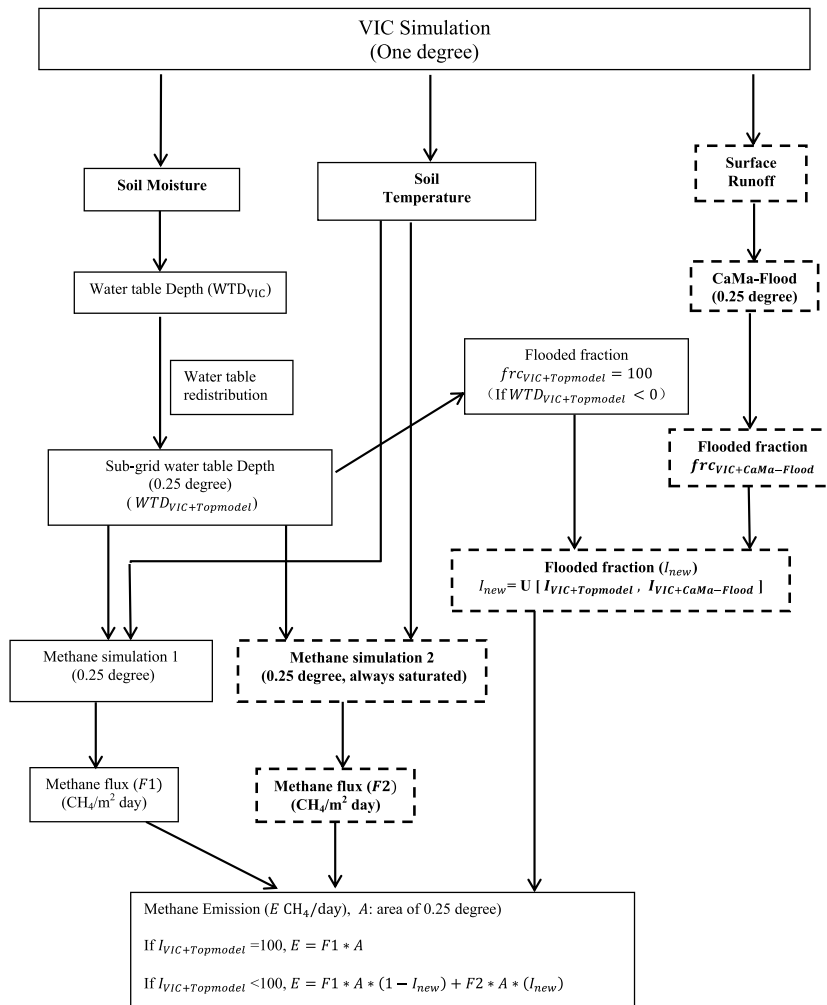
Figure 1. Flowchart to estimate the inundation extent and methane emissions in this study. The components with bold and dashed frame are the parts we newly added to capture the effect of surface water flow on methane emissions.

each 0.25° grid cell: the first rate ($F1$) is calculated assuming that the whole cell is noninundated and the second rate ($F2$) is calculated assuming that the whole grid cell is inundated (Figure 1).

The methane emission for a 0.25° grid cell is then estimated as the sum of emissions from its inundated and noninundated parts ($E = F1 \times A \times (1 - I_{new}) + F2 \times A \times I_{new}$). Note that the water table for its unsaturated part ($1 - I_{new}$) is still estimated from the TOPMODEL-based redistribution. In this way, the new methane model can capture small variations in inundation extent which is finer than the 0.25° resolution (depending on its significant figure). The assumption needed here is that soil column under inundated surface is always saturated, which may lead to the biases in the very short time simulation. However, this is not an unreasonable assumption, and the possible negative effects should be minor in this daily study.

3. Simulation Settings and Input Data

The global 1° daily runoff from 2005 to 2010 was generated from the VIC simulation which was used as the input for the CaMa-Flood model simulation. The required input data for the VIC model including gridded daily precipitation, maximum and minimum daily air temperatures, and wind speed were acquired from the National Centers for Environmental Prediction atmospheric reanalysis [*Kalnay et al.*, 1996]. Soil hydraulic parameters [*Nijssen et al.*, 2001] and other vegetation parameters such as minimum stomatal resistance, albedo, and rooting depth and fraction specified for each vegetation class were obtained from the VIC model website (http://www.hydro.washington.edu/Lettenmaier/Models/VIC/). The land cover map was obtained

Table 1. Comparison of the Daily River Discharge in the Selected Major Basins[a]

Basin	Station	Latitude	Longitude	Area ($10^3 km^2$)	Period	Q_{obs}	Q_{sim}	R
Amazonas	Obidos-Linigrafo	−1.9192	−55.513	4680	2007	173964	124356	0.65
Congo	Kinshasa	15.3	3475000	3475	2006–2010	40050	50051	0.71
Ob	Salekhard	66.57	66.53	2950	2006–2010	12693	16597	0.76
Mississippi	Baton Rouge	32.31	−90.91	2916	2006–2010	14965	20305	0.78
Parana do Careiro	Careiro	−3.1961	−59.834	2583	2006–2009	13376	9701	0.72
Yenisei	Igarka	67.48	86.5	2440	2006–2010	20208	17132	0.81
Lena	Kyusyur	70.7	127.65	2430	2006–2010	20207	17057	0.83
Mackenzie	Arctic Red River	67.4583	−133.74	1660	2006–2010	10087	13601	0.79
Yukon	Pilot Station	61.93	−162.88	831	2006–2010	6784	7891	0.80
Columbia	The Dalles	45.61	−121.17	614	2006–2010	5085	5689	0.82
Ohio	Metropolis	37.13	88.73	526	2006–2010	8685	6501	0.73

[a]Q_{obs} and Q_{sim} are the annual average discharge (m^3/s) for observation and simulation, respectively. R is the correlation coefficient, estimated from the daily values. The Amazonas and Parana do Careiro Basins are in the Southern Hemisphere, and the rest of the basins are in the Northern Hemisphere.

from the University of Maryland's 1 km Global Land Cover product [*Hansen et al.*, 2000] and processed to build the vegetation fraction data set in each 1° simulation grid.

The CaMa-Flood model was also run for the period from 2005 to 2010. The first year, 2005, was used as a spin-up period and excluded for the further analysis. In this study, we run the CaMa-Flood model at the 0.25° spatial resolution and an adaptive time step. The required input data for the CaMa-Flood model including the global digital elevation model and its derivatives, flow direction map, river width length, and height are distributed with the model package (http://hydro.iis.u-tokyo.ac.jp/~yamadai/cama-flood).

The input data for the methane module include the daily net primary production (NPP), the land cover types [*Melillo et al.*, 1993], soil texture [*Zhuang et al.*, 2003], and soil-water PH [*Carter and Scholes*, 2000]. The daily NPP was derived from the MODIS NPP monthly product (MOD17A2) and was assumed to be the same through 1 month. Also see the supporting information for the input data.

4. Results and Discussions

We first evaluated the model's performance in simulating discharge, flooded extent, and methane emissions. Then we investigated the effects of incorporating the CaMa-Flood model by comparing against the results from our previous model and other models.

4.1. Evaluations

We compared the simulated daily river discharge in eleven major river basins against observations at the gauging stations. For each river, the gauging station with available measurements in the study period and also located the farthest downstream were selected. The location of the gauging stations (latitude and longitude), upstream drainage area ($10^3 km^2$) and the period used are shown in Table 1. We also calculated the correlation coefficient, R, from the daily observations and simulations in Table 1. The data for the stations in the U.S. were acquired from the U.S. Geological Survey, and the rest were provided by the Global Runoff Data Center, available at http://www.bafg.de/GRDC/.

Annual average discharge for most rivers in the Northern Hemisphere was overestimated using our I_{new} based framework and was underestimated for the rivers in the Southern Hemisphere (Table 1). The framework can roughly capture the seasonal pattern of the river discharge with the correlation coefficient in the range between 0.65 and 0.83. Its performance is affected not only by the algorithm and elevation-derived data used in the CaMa-Flood model but also the runoff from the VIC model. It is noted that given limited information on global infrastructure, we did not account for the river discharge regulation by the dams. This is a common assumption in other large-scale studies [e.g., *Wu et al.*, 2014; *Nguyen et al.*, 2015].

We also evaluated the simulated flooded extent by comparing with the GIEMS data [*Prigent et al.*, 2007; *Papa et al.*, 2010] and SWAMPS dataset [*Schroeder et al.*, 2015]. From the optical, passive and active microwave data, the GIEMS provides global monthly inundated extent at the 25 km resolution from 1993 to 2007. SWAMPS
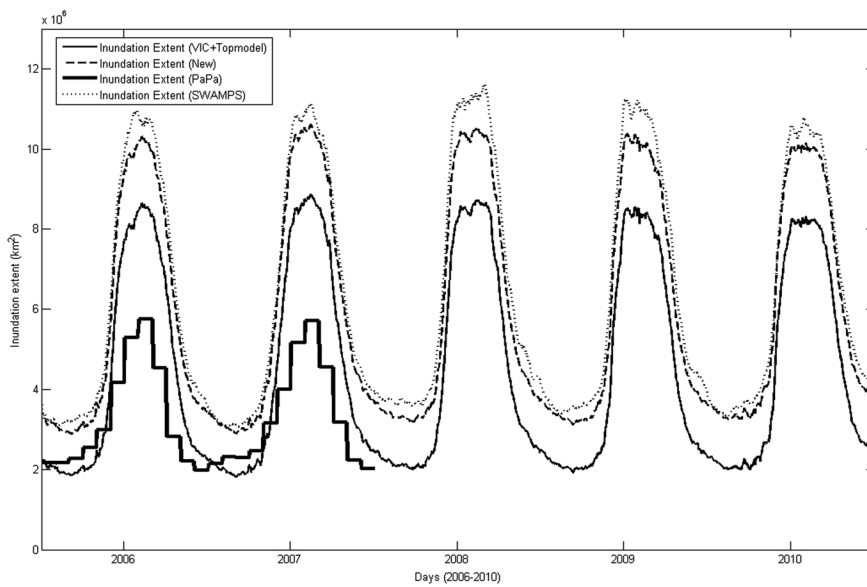
Figure 2. Global daily flooded area estimated from $I_{\text{VIC + Topmodel}}$, I_{new} (dashed), and multisatellite observations (PaPa, bold). Note that the temporal resolution of satellite observations is monthly and the two simulations are daily time step.

provides a global daily inundation by combining passive/active microwave remote sensing data from 1992-2013 at a 25 km resolution. The time series of global floodplains from the simulations ($I_{\text{VIC + Topmodel}}$ and I_{new}) and the satellite observation were compared (Figure 2). The seasonal pattern of the simulated inundated area matches well with the satellite observations. The inundation extent is larger in the two model simulations than that from the multisatellite observation: the GIEMS data report a maximum inundation extent of $5.6 \times 10^6 \text{ km}^2$ during the study period, while our estimation is close to $11.0 \times 10^6 \text{ km}^2$ (I_{new}) and $8.5 \times 10^6 \text{ km}^2$ ($I_{\text{VIC + Topmodel}}$), respectively. The underestimation of the satellite-derived inundation extent is mainly due to the low sensitivity of the retrieval algorithm in detecting small flooded area [*Prigent et al.*, 2007; *Yamazaki et al.*, 2011] and the low temporal resolution which may report minimum inundation extent in one month. However, the new inundation extent from SWAMPS has much higher temporal resolution. It is in good agreement with our simulated result: the annual maximum inundated area for the global domain estimated from SWAMPS is $11.9 \times 10^6 \text{ km}^2$ during 2006–2010, which is less than 10% higher than our estimation.

We validated our algorithms for the methane production and consumption at the site level in previous studies by comparing against the measurements [*Lu and Zhuang*, 2012; *Zhu et al.*, 2014]. In this study, we evaluated the new methane model on a large scale. However, it is important to note that both the forward and inverse models highly depend on their assumptions and parameters; thus, none of their results can be used as the unbiased data set. Also as indicated in the WETCHIMP study [*Melton et al.*, 2013], the global CH_4 observations have large uncertainties and the lack of reliable global data sets limits efforts to evaluate methane models' performance. However, some regions have the airborne-based CH_4 observations. For example, the annual methane emissions in the Hudson Bay lowland (HBL) were measured by aircrafts [*Harriss et al.*, 1994; *Roulet et al.*, 1994; *Worthy et al.*, 2000; *Pickett-Heaps et al.*, 2011] during the period 2004–2008. Most other models reported HBL as a methane source emitting 2.9–11.3 $\text{Tg CH}_4 \text{ yr}^{-1}$ (Table 3). Although simulated in different periods, the results from $I_{\text{VIC + Topmodel}}$ and I_{new} fall in the range of measured methane emissions: 7.9 ± 1.2 and 10.9 ± 1.3 $\text{Tg CH}_4 \text{ yr}^{-1}$ (Table 3), respectively. Another region with methane emissions measurements is the West Siberian Lowlands (WSL) [*Winderlich et al.*, 2010; *Glagolev et al.*, 2011]. The reference observations in WSL were developed by combining the in situ chamber observations and the statistical model of methane fluxes as function of wetland types. According to this observation data set, 3.92 ± 1.29 $\text{Tg CH}_4 \text{ yr}^{-1}$ were emitted from the WSL during 1993–2004. WSL was estimated by our methane model ($I_{\text{VIC + Topmodel}}$) as a methane source with a magnitude of 8.74 $\text{Tg CH}_4 \text{ yr}^{-1}$ for the same period. The I_{new} proposed in this study gives a higher estimate of 11.7 $\text{Tg CH}_4 \text{ yr}^{-1}$ for the period of 2006–2010. Given that the current methane models are different in estimating the inundation extent (Table 2), the modeled methane emissions can be more different among them. However,

Table 2. Comparison of the Mean Annual Maximum Inundation Extent From the Models

Model	Resolution (Longitude × Latitude)	Global Maximum Inundation Extent (10^6 km²)	Tropics (30°S–30°N) (10^6 km²)	Extratropics (> 35°N) (10^6 km²)	Period	References
CLM4Me	2.5° × 1.9°	8.8 ± 1.5	2.6 ± 0.2	5.1 ± 1.4	1993–2004	*Riley et al.* [2011]
DLEM	0.5° × 0.5°	7.1 ± 1.1	3.1 ± 0.4	3.3 ± 0.8	1993–2004	*Tian et al.* [2011]; *Xu and Tian* [2012]
GIEMS[a]	0.25° × 0.25°	12.6 ± 0.8	6.0 ± 1.4	5.2 ± 1.2	1993–2004	*Melton et al.* [2013]
GIEMS	0.25° × 0.25°	5.6 ± 0.8	2.7 ± 0.1	2.7 ± 0.0	2006–2007	*Prigent et al.* [2012]
LPJ-Bern	0.5° × 0.5°	81.7 ± 2.4	38.8 ± 1.8	36.4 ± 2.8	1993–2004	*Spahni et al.* [2011]
LPJ-WHyMe	0.5° × 0.5°	2.7	NA	NA	1993–2004	*Wania et al.* [2010]
LPJ-WSL	0.5° × 0.5°	9.0 ± 1.1	3.8 ± 0.3	4.2 ± 0.9	1993–2004	*Hodson et al.* [2011]
ORCHIDEE	1.0° × 1.0°	8.6 ± 0.9	4.3 ± 0.3	3.4 ± 0.7	1993-2004	*Ringeval et al.* [2011, 2012]
SDGVM	0.5° × 0.5°	26.9 ± 3.6	13.2 ± 1.1	12.0 ± 3.8	1993–2004	*Hopcroft et al.* [2011] *Singarayer et al.* [2011]
UVic-ESCM	3.6° × 1.8°	16.3 ± 1.4	10.6 ± 0.4	5.0 ± 1.2	1993–2004	*Avis et al.* [2011]
VIC + Topmodel	0.25° × 0.25°	8.5 ± 2.2	1.4 ± 0.1	6.7 ± 0.1	2006–2010	*Lu and Zhuang* [2012]
VIC + Topmodel + CaMa	0.25° × 0.25°	10.6 ± 1.9	2.1 ± 0.1	7.9 ± 0.2	2006–2010	This study

[a]The GIEMS inundation data set contain rice agriculture.

the higher methane emissions from the $I_{VIC+Topmodel}$, which has similar inundation extent to other models, suggest that our algorithms and parameters controlling methane production, oxidation, and transport could be one of factors leading to the higher estimation. The I_{new} with even larger flooded areas tends to have higher estimation of methane emissions than other models.
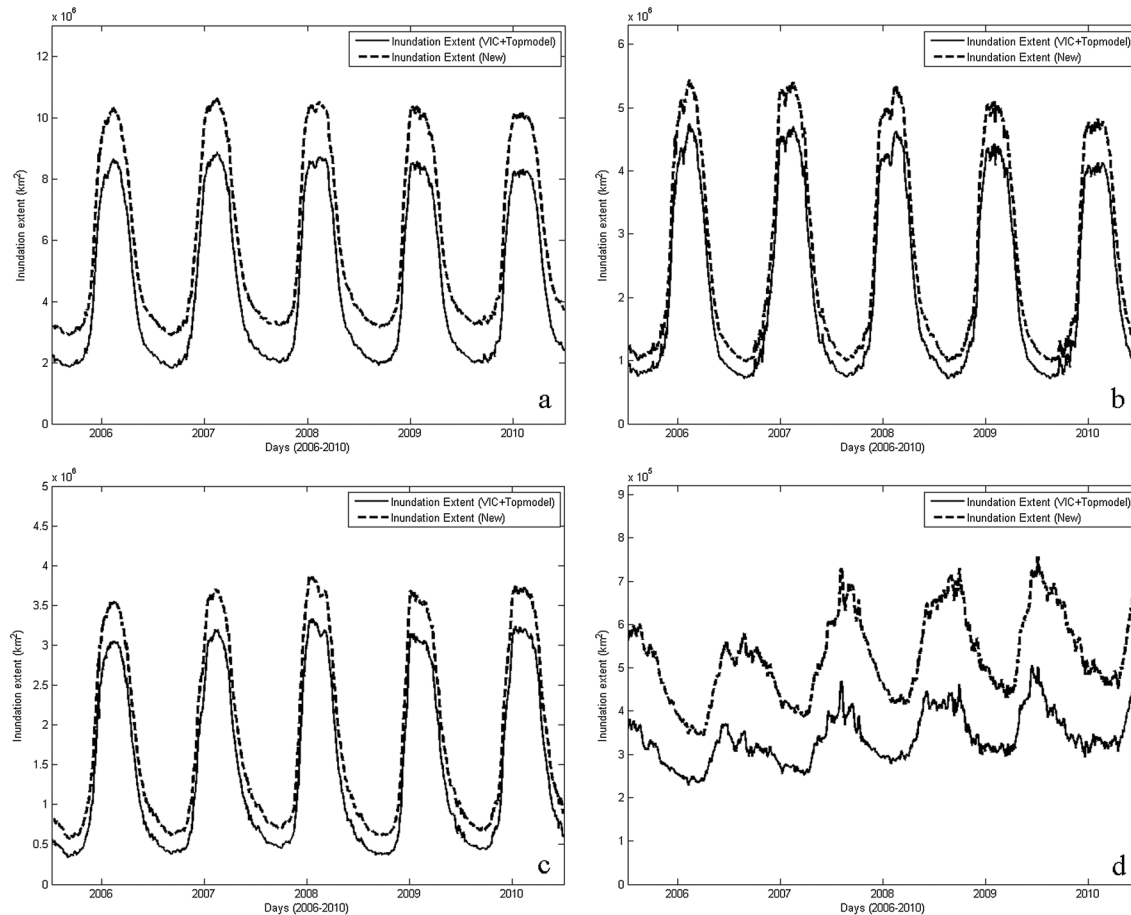
Figure 3. Comparison of the daily inundation extent in the (a) global, (b) Asia, (c) North America, and (d) South America estimated by the $I_{VIC+Topmodel}$ (solid line) and I_{new} (dash).

4.2. Inundation Extent

The daily inundation extent estimates in continents with large flooded area including Asia, North America, South America, and global from the $I_{VIC + Topmodel}$ and the I_{new} are illustrated in Figure 3. During 2006–2010, the global maximum and minimum flooded areas from the I_{new} are 1.0×10^7 km^2 and 2.8×10^6 km^2, respectively (Figure 3a). Both of them are approximately 1.0×10^6 km^2 larger than those from $I_{VIC + Topmodel}$. The fundamental reason for the difference is how surface runoff contribution to the inundation extent is assumed in the two schemes: $I_{VIC + Topmodel}$ lacks the ability to represent horizontal water movement, and its saturated area is determined only by water balance in a local grid, while I_{new} estimates inundation extent from both soil moisture and water transport. Therefore, the two schemes report large difference of flooded areas in summer and winter periods. The large difference in summer is mainly due to snow melting in Asia (Figure 3b) and North America (Figure 3c): snow melt usually leads to floods in spring and the early summer time; the disagreement in winter time is the result of heavy precipitation in tropical regions, such as South America (Figure 3d). The large difference of estimated inundation extent from these two schemes in South America lasts almost all year round. The reasons are (1) the runoff does not rely on snow melt and (2) some large basins, such as parts of Amazon Basin, are relatively flat and the inundation duration can last longer than other regions.

The spatial distribution of the inundation area during the period 2006–2010 estimated from $I_{VIC + Topmodel}$, I_{new}, and their difference are shown in Figure 4. Note that the inundation fraction from $I_{VIC + Topmodel}$ is binary values: 0 (no inundated) or 1 (inundated). Snow melt is the major factor influencing the inundation extent, especially in Northern Asia and North America. In fact, the inundated area detected by the $I_{VIC + Topmodel}$ is mostly likely located in the place where the I_{new} also reported 100% inundated. The explanation is that the inundated area estimated from $I_{VIC + Topmodel}$ is primarily determined by the soil moisture and topographic information (Figure 4a) which are also considered in the I_{new}. The places where estimations from these two schemes are different (Figure 4c) usually have the inundation fraction around 30% or below and are even the upland areas with short flood duration. The $I_{VIC + Topmodel}$ has no mechanism for the surface lateral flow, and thus, it can only capture the inundation extent in the lowland areas, while I_{new}, as we can see in the Figure 4b, cannot only capture the lowland inundated areas but also track the short-term flooded upland areas. This point is particularly distinct in Australia: only a small fraction of Northern Australia was saturated according to the $I_{VIC + Topmodel}$, while most arid regions, mainly in the western and southern part, were never saturated during the study period (Figure 5a); I_{new} reported more inundated areas (Figure 5b) with short duration, less than 10 days in 1 year.

The I_{new} also performs differently compared to the $I_{VIC + Topmodel}$ in the flat regions as shown in western Europe and Eastern China. Both of the two regions are relatively flat and the inundated areas mainly located along the downstream areas of the Danube River (Figure 5c) and the Yangtze River (Figure 5e), respectively. The performance of the TOPMODEL-based water table redistribution method is reduced due to the relative coarse resolution and flat topography: $WTD_{VIC + Topmodel}$ is almost equal to WTD_{VIC} everywhere except in regions with a large upstream drainage area.

The mean annual maximal inundation extent from eight models in WETCHIMP was compared in Table 2: CLM4Me [*Riley et al.*, 2011], DLEM [*Tian et al.*, 2011; *Xu and Tian*, 2012], LPJ-Bern [*Spahni et al.*, 2011], LPJ-WHyMe [*Wania et al.*, 2010], LPJ-WSL [*Hodson et al.*, 2011], ORCHIDEE [*Ringeval et al.*, 2011, 2012], SDGVM [*Hopcroft et al.*, 2011; *Singarayer et al.*, 2011], and UVic-ESCM [*Avis et al.*, 2011]. LPJ-WHyMe is the only model using static inundation extent; two models, SDGVM and UVic-ESCM, fully rely on their hydrological modules to determine the saturated areas, and the rest of the five models used the GIEMS data set to represent their inundation distribution. More details about model difference can be found in Wania et al.'s paper [*Wania et al.*, 2013]. The GIEMS values used in the Melton's study [*Melton et al.*, 2013] (also Table 2) is annual maximum wetland extent which is the sum of annual maximum inundated areas for all grid cells. Thus, the inundated area, 12.6×10^3 km^2, is much higher than that in Figure 2 ("Inundation extent PaPa"). LPJ-Bern has significantly higher inundation extent than other models and observations. The soil parameterization used in this model is likely the main reason for this overestimation [*Melton et al.*, 2013]. The two models, SDGVM and UVic-ESCM, also report the relatively larger flooded areas possibly due to the simple hydrological modules [*Melton et al.*, 2013]. The other models constrained by the GIEMS observation simulated the inundation extent in the range from 7.1 to 9.0×10^6 km^2, which is below the maximum inundated area from the GIEMS.
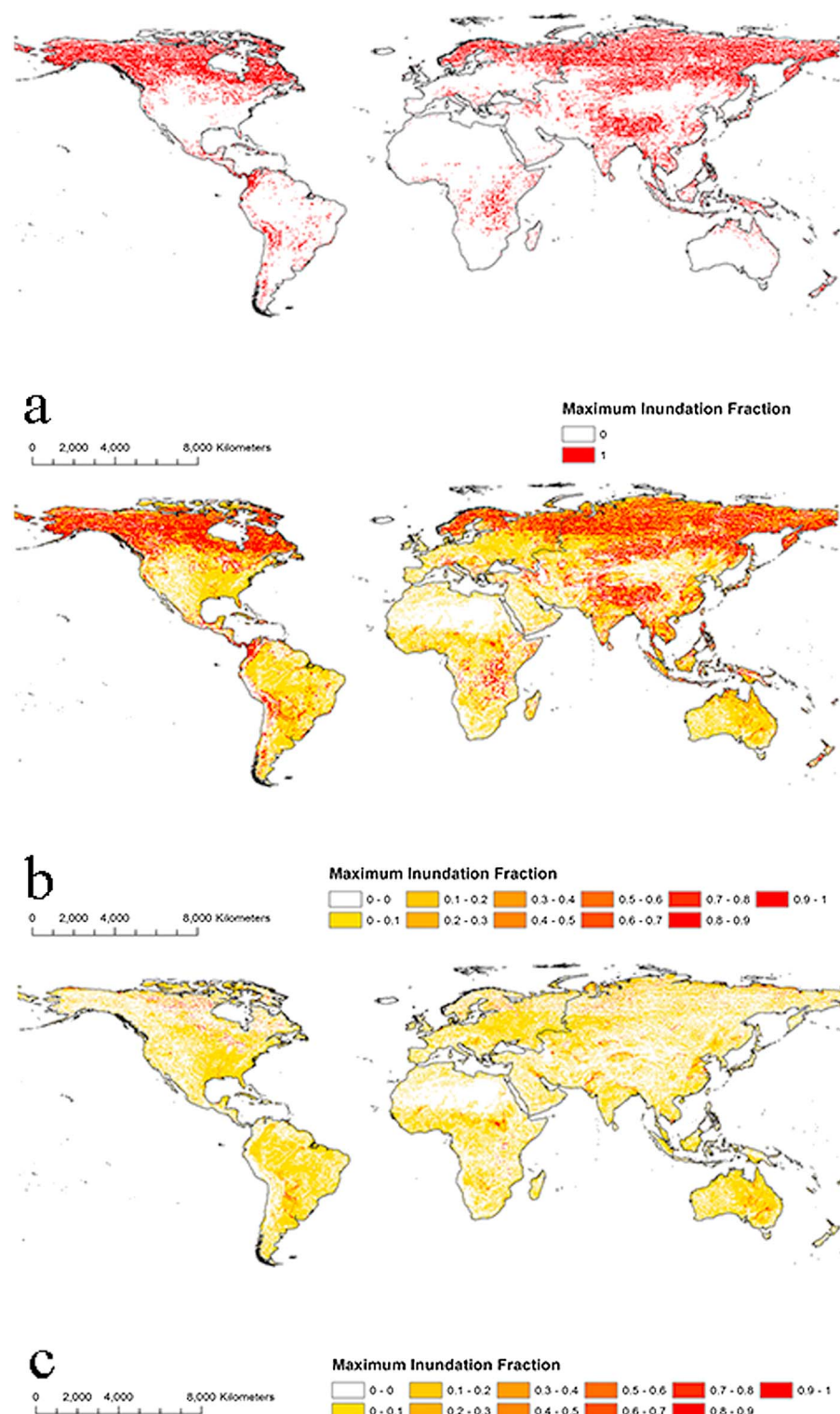
Figure 4. Spatial distribution of the mean maximum inundation extent during the period 2006–2010 estimated from the (a) $I_{VIC + Topmodel}$, (b) I_{new}, and their (c) difference ($I_{new} - I_{VIC + Topmodel}$).
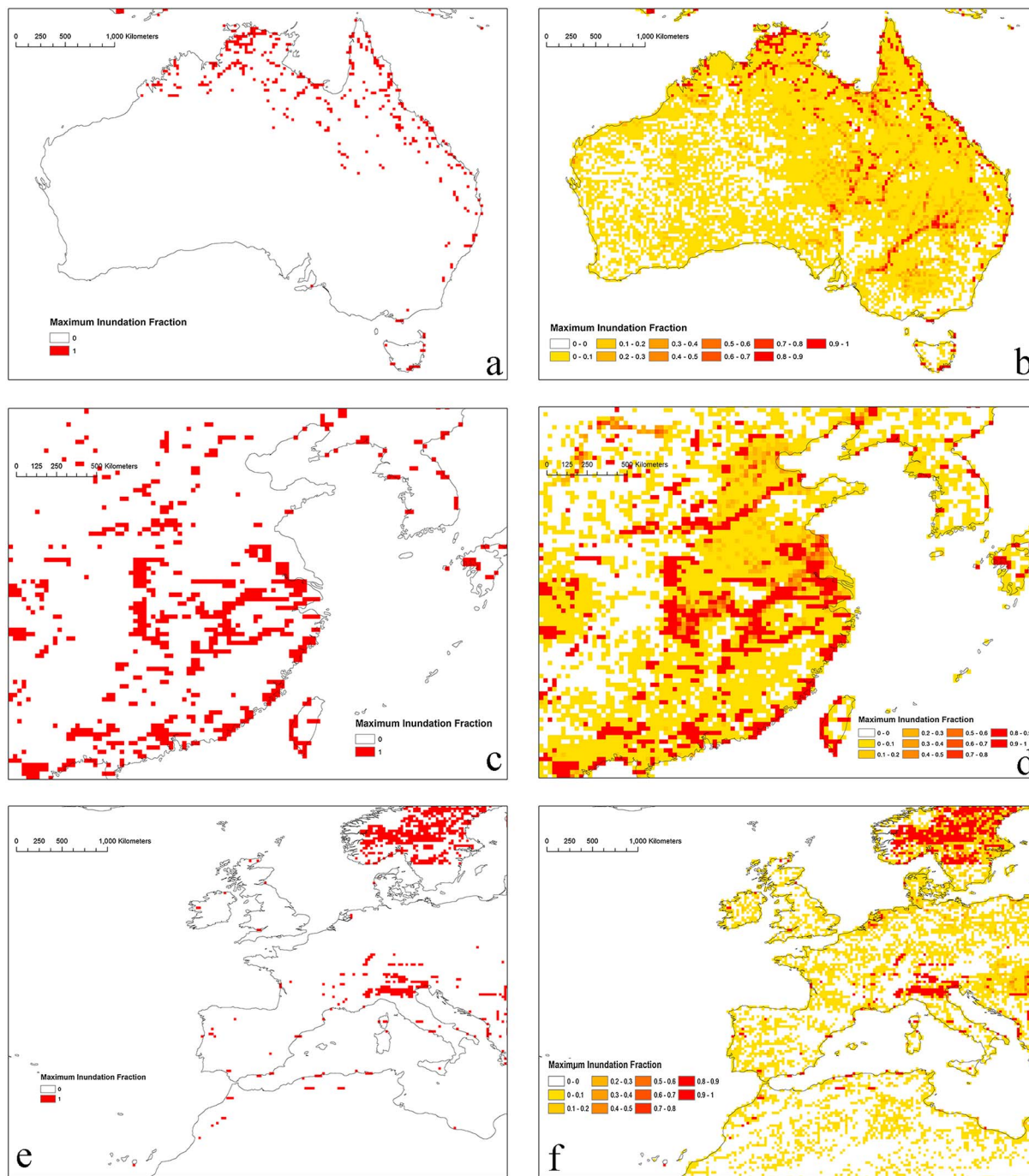
Figure 5. Comparison of the spatial distribution of the mean annual maximum inundation extent during 2006–2010 estimated from the $I_{VIC + Topmodel}$ in (a) Australia, (c) Eastern China, and (e) western Europe and the I_{new} in (b) Australia, (d) Eastern China, and (f) Western Europe.

The inundated areas simulated from $I_{VIC + Topmodel}$ and I_{new} are $8.7 \pm 2.2 \times 10^3$ and $10.9 \pm 1.9 \times 10^3$ km², respectively. With consideration of water flow from upland areas, the I_{new} has a larger estimation of inundated area than $I_{VIC + Topmodel}$ (Table 2) and most of the other models. We noticed that 80% of the inundated areas from the I_{new} located in the extratrophic region (>35°N, Table 2) and the high-latitude regions contribute a large fraction. Also, the inundated area in the trophic region (30°S–30°N) is smaller than most of the other studies. In our simulation, many high-latitude regions have high soil moisture due to the low evapotranspiration; the ice melt in the spring leads to the large-scale flood. The inundation extent could be different because of model's assumptions,

Table 3. Simulated Annual Mean Methane Emissions (Tg CH_4 yr^{-1})[a]

Model	Resolution (Longitude × Latitude)	Global	Tropics[b]	Extratropics[c]	HBL[d]	Period	References
CLM4Me	2.5° × 1.9°	206 ± 6	134 ± 5	62 ± 6	3.4 ± 0.3	1993–2004	*Riley et al.* [2011]
DLEM	0.5° × 0.5°	141 ± 11	85 ± 7	39 ± 3	2.9 ± 0.2	1993–2004	*Tian et al.* [2011] and *Xu and Tian* [2012]
LPJ-Bern	0.5° × 0.5°	181 ± 15	106 ± 2	65 ± 13	11.3 ± 7.9	1993–2004	*Spahni et al.* [2011]
LPJ-WHyMe	0.5° × 0.5°			27 ± 2	5.5 ± 1.0	1993–2004	*Wania et al.* [2010]
LPJ-WSL	0.5° × 0.5°	174 ± 10	122 ± 7	42 ± 2	3.9 ± 0.3	1993–2004	*Hodson et al.* [2011]
ORCHIDEE	1.0° × 1.0°	264 ± 12	184 ± 11	71 ± 4	9.1 ± 1.7	1993–2004	*Ringeval et al.* [2011, 2012]
SDGVM	0.5° × 0.5°	199 ± 5	135 ± 6	59 ± 3	2.2 ± 0.2	1993–2004	*Hopcroft et al.* [2011] *Singarayer et al.* [2011]
$I_{VIC + Topmodel}$	0.25° × 0.25°	227 ± 9	81 ± 7	129 ± 6	7.9 ± 1.2	2006–2010	*Lu and Zhuang* [2012]
I_{new}	0.25° × 0.25°	297 ± 11	126 ± 9	141 ± 7	10.9 ± 1.3	2006–2010	This study
			Inverse Model Estimation				
Bloom 2010	3° × 3°	171 ± 52	92 ± 28	74 ± 22	4.9 ± 1.4	2003–2007	*Bloom et al.* [2010]
Bousquet2011[R]	1° × 1°	145 ± 10	91 ± 11	43 ± 4		1993–2009	*Bousquet et al.* [2006, 2011]
Bousquet2011[K]	1° × 1°	151 ± 10	97 ± 10	43 ± 4		1993–2009	*Bousquet et al.* [2006, 2011]

[a]The standard deviation represents the interannual variation in the model estimates. *R* and *K* are global inversions using LMDZ with emissions from *Matthews and Fung* [1987] and *Kaplan* [2002] as the wetland prior, respectively.
[b]30°S–30°N.
[c]>35°N.
[d]50°N–60°N, 75°W–96°W.

algorithms, boundary conditions, and parameters. Above analysis shows that it is helpful with our new incorporation of surface water movement to capture inundated areas occurring in flat and arid regions.

4.3. Methane Emissions

4.3.1. CH_4 Emissions

The annual global methane emitted to the atmosphere for the period 2006–2010 is estimated to be 297 ± 11 and 227 ± 9 Tg CH_4 yr^{-1} by the I_{new} and $I_{VIC + Topmodel}$, respectively. Although our estimate from $I_{VIC + Topmodel}$ is within the range of the selected forward model results which are between 141 and 264 Tg CH_4 yr^{-1} (Table 3), its estimation is higher than all the model's results except ORCHIDEE. The I_{new}, however, gave an estimate about 30% higher than $I_{VIC + Topmodel}$, which is expected because the inundation extent from the I_{new} is broader than that from the $I_{VIC + Topmodel}$. As indicated in the evaluation section, we tend to give high methane emission estimation using I_{new} due to the increase in inundation extent and the methane module. The simulation based on the I_{new} reports that the trophic region contributes less emissions than the extratrophic region (126 Tg CH_4 yr^{-1} versus 141 Tg CH_4 yr^{-1}) (Table 3), which is contrary to most of the other models. The difference in their hydrological modules is one of the reasons that the VIC has the comprehensive mechanism to track the dynamic of snow pack and the phase change of soil moisture. The effect of spring flood occurring in high latitudes is well considered in the VIC model, while some of the other models may underestimate this effect due to the lack of soil thermal component.

4.3.2. Spatial Distribution of Methane Emissions

As expected, the spatial pattern of methane emissions is highly dependent on the distribution of inundated area (Figure 6). In high-latitude regions, previous studies [*Rofaier et al.*, 2013; *Zakharova et al.*, 2013] have shown that soil moisture (ice or liquid water) is usually at relatively high level. With temperature increase in summer time, ice melt in soil and the thawing of snowpack lead to large-scale saturated zones. Moreover, the low loss from evapotranspiration keeps soil moisture at high level until soil frozen in late September or October.

On the other hand, the soil moisture estimated from VIC simulation is relatively low in the trophic region, due to high evapotranspiration loss. Contrary to other methane models, this study shows that the methane emissions in the trophic region are slightly lower than that in the extratrophic region. The soil moisture in the trophic region is largely determined by precipitation and evapotranspiration. Different from the high latitudes with water stored in soil, soil moisture in the low latitudes will decrease rapidly when rainfalls stop. The strong methane emission zones are usually located in places near to river networks where soil can get water supply from flood water regularly.

The distribution of mean methane emission during 2006–2010 in Australia, Eastern China, and western Europe is shown in Figure 7. Although the methane emissions in Australia from the I_{new} show broader extent than that from the $I_{VIC + Topmodel}$ (Figure 6), the flux intensity in the new source areas is usually at a low level because most of them are located in the western arid region with poor organic substrate availability. Also,
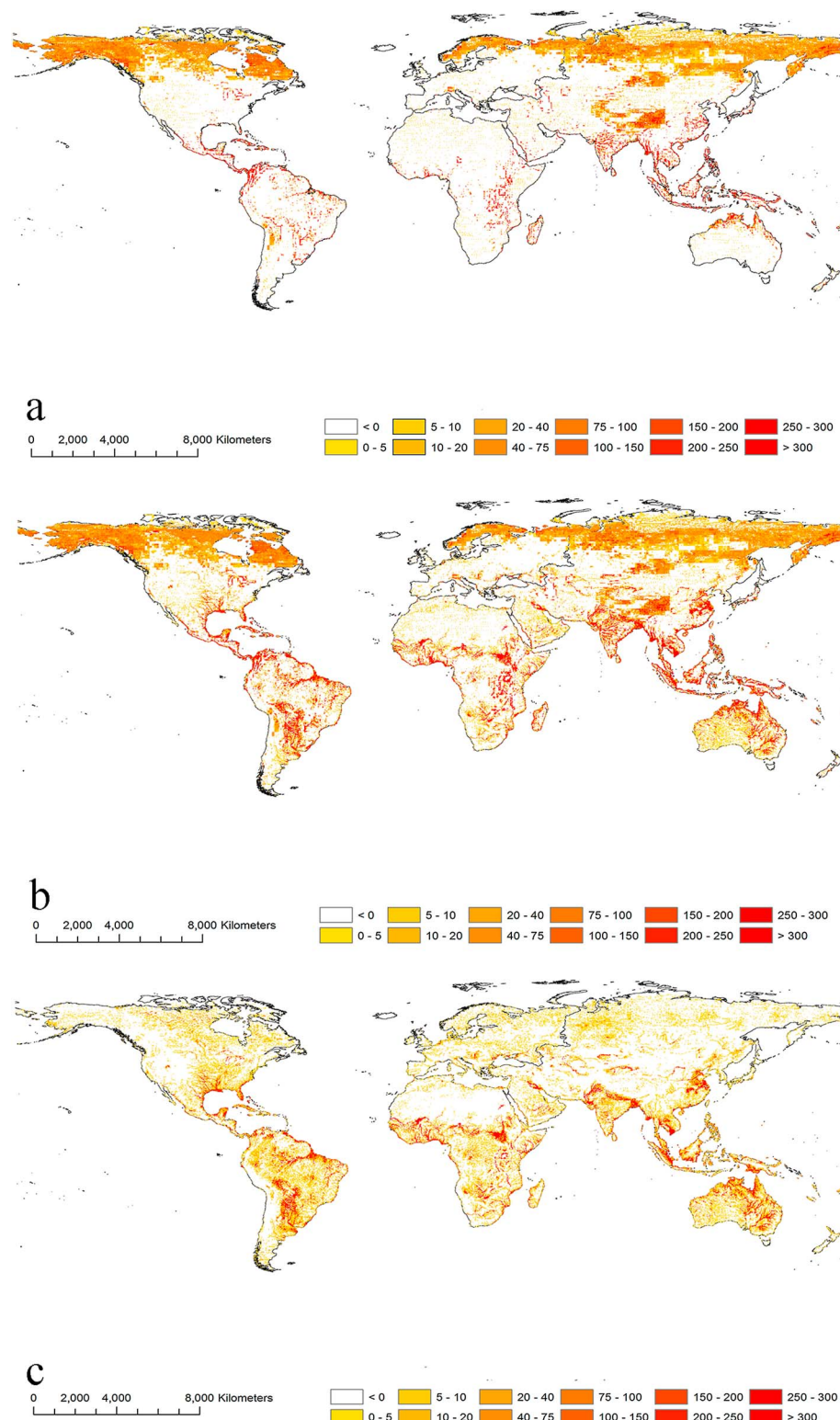
Figure 6. Spatial distribution of the mean methane emissions estimated from (a) $I_{VIC + Topmodel}$, (b) I_{new}, and (c) their difference ($I_{new} - I_{VIC + Topmodel}$) during the period of 2006–2010. The unit is g CH_4/m^2 yr.
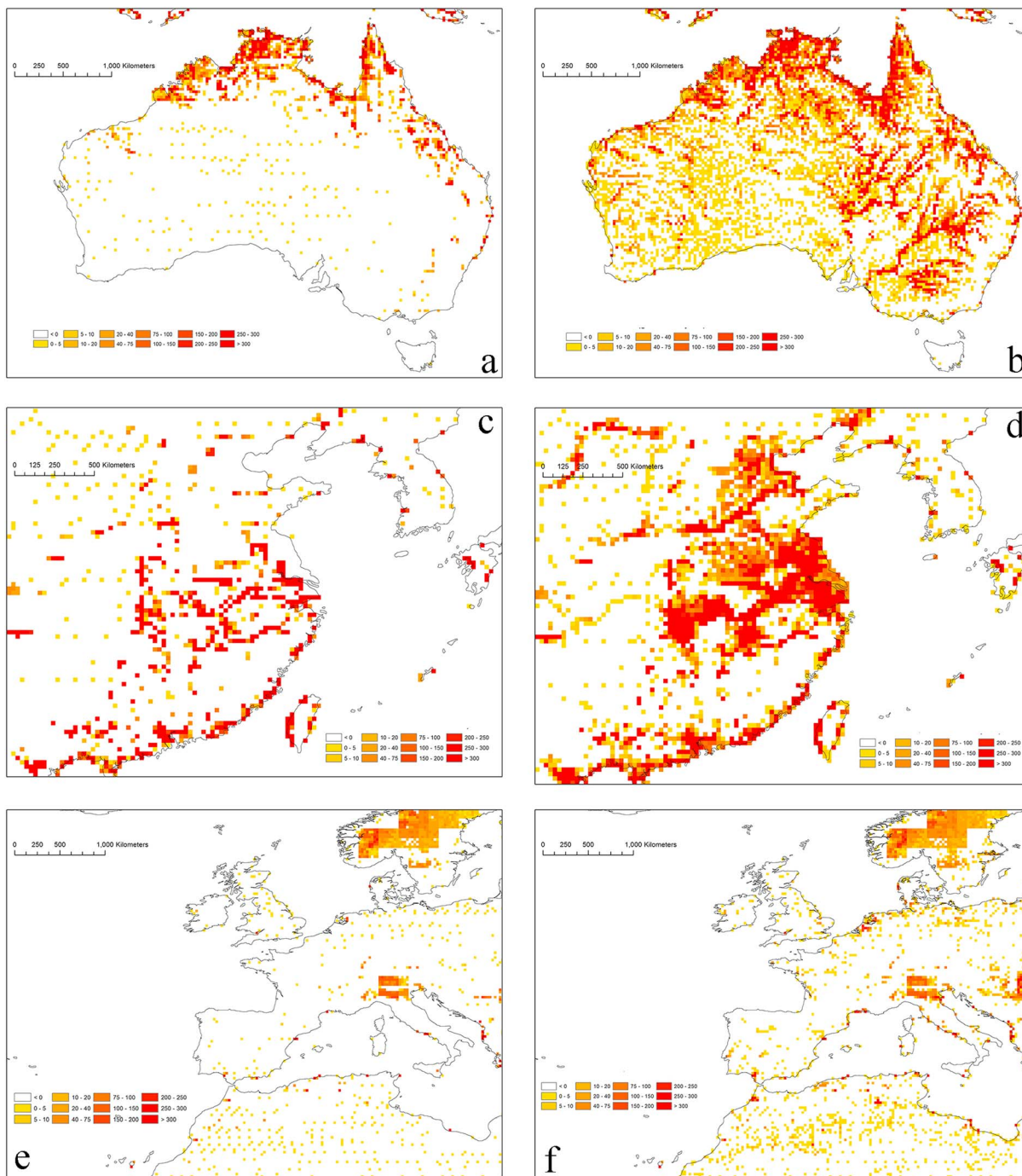
Figure 7. Comparison of the spatial distribution of the mean methane emissions during 2006–2010 estimated from the $I_{VIC + Topmodel}$ in (a) Australia, (c) Eastern China, and (e) western Europe and from the I_{new} in (b) Australia, (d) Eastern China, and (f) western Europe. The unit is g CH_4/m^2 yr.

precipitation is low and evapotranspiration is high in most new inundated areas, which lead to a short duration of inundation. These factors contribute to significant increase of total methane emissions in Australia with incorporation of the surface routing module. The annual methane emissions from the $I_{VIC + Topmodel}$ and I_{new} during the study period are estimated to be 6.8 and 11.5 Tg CH_4/yr, respectively.

Following the inundation extent pattern in Eastern China, the methane source area from the I_{new} is also larger than that from the $I_{VIC + Topmodel}$ (Figure 7). Although the high methane emissions zone around the Yangtze River can be roughly recognized from the methane emissions map generated from the $I_{VIC + Topmodel}$, it is
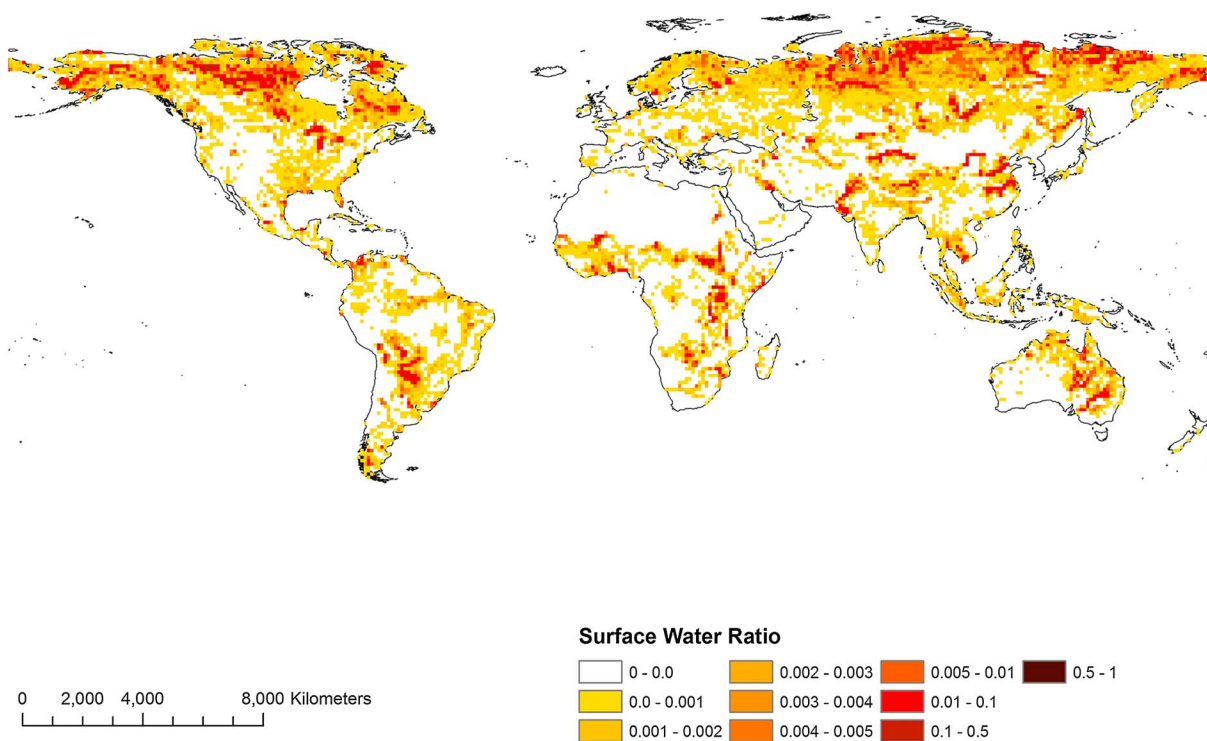
Figure 8. Mean ratio between surface water and soil liquid water during 2006–2010.

hard to differentiate the channel networks of the Yellow River and Pearl River from this map. It suggests that the TOPMODEL-based method at the 0.25° resolution may be still limited in terms of topographic heterogeneity. The inundation areas derived from the I_{new}, however, clearly illustrate most channel nodes of the Yellow River, the Yangtze River, and the Pear River (Figure 5). Particularly, there is a large methane source region locating in the Middle-Lower Yangtze Plain due to the East Asian rainy season while this region is barely shown in the map generated from the $I_{VIC + Topmodel}$. The flat topography limits the performance of the $I_{VIC + Topmodel}$, and the water table depth is almost equal to the uniform one estimated directly from the VIC simulation. The map from the I_{new} has the same spatial resolution to that from the $I_{VIC + Topmodel}$, each grid cell, however, has a inundated fraction rather than a binary inundated flag used in the $I_{VIC + Topmodel}$. This feature can significantly improve the model to capture the local heterogeneity without increasing the grid cell's resolution and computing time. At the same time, relatively dense vegetation in Eastern China produces enough organic substrate availability for methane production. Therefore, similar to Australia, methane emissions are larger with consideration of surface water in Eastern China: 5.4 and 7.2 Tg CH_4/yr during 2006–2010 from the $I_{VIC + Topmodel}$ and I_{new}, respectively.

The terrain in western Europe is generally flat and undulating, but there is no intense rainy season. The extent of flooded area is relatively small and less variant. Although there are large inundated areas reported by the GIEMS data set, most of them are flooded agricultural lands rather than natural wetlands [*Melton et al.*, 2013]. Surface water does not have the similar duration and extent compared to that in Eastern China; thus, the surface water routing did not lead to large difference in the methane emissions between $I_{VIC + Topmodel}$ and I_{new}. It emits 0.6 and 0.1 Tg CH_4/yr during 2006–2010 from the $I_{VIC + Topmodel}$ and I_{new}, respectively. In addition to Northern Italy, which is found to be a major methane source by the $I_{VIC + Topmodel}$ and I_{new} (Figure 7e), another high flux region around the outlet of the Danube River is found in the I_{new} simulation (Figure 7f).

4.3.3. Contribution of Surface Water to Inundation Extent and Methane Emissions

Since liquid water plays an important role in the methane emissions, we calculated the mean ratio between liquid water stored in ground surface (not including river water and lake water) and that in soil (in upper 1.6 m soil layer) in summer time of the study period. The spatial distribution of this ratio was shown in Figure 8. Surface water only occupies a small fraction of the total liquid water storage, about 1.28% for

the global during 2006–2010. Surface water contributes a higher fraction in high-latitude regions due to relatively higher ice content in soil and large melted water from snowpack. Surface water also occupies a relatively higher fraction in areas close to streams. When the surface water is taken into account in estimating inundation extent, it leads to 24.7% and 30.8% increases in the maximum inundation extent and methane emission in the global scale. It indicates that although surface water is a relatively small component in the terrestrial water balance, it can play a significant role in controlling the inundation extent and the methane emissions.

The importance of surface water varies in different regions: (1) while difference in inundated areas from the I_{new} and $I_{VIC + Topmodel}$ is considerably large in many regions, their difference in inundated fraction is relatively small in the high-latitude regions. The reason is that most of the soil is already saturated due to the melting of soil ice in summer and surface snowpack and runoff is mainly generated by saturation excess (Dunne runoff [*Dunne and Black*, 1970a, 1970b; *Dunne et al.*, 1991]). Both the I_{new} and $I_{VIC + Topmodel}$ can capture most of such inundated areas, the difference mainly occurs in the uplands; (2) most differences from two schemes occur in flat and humid regions with heavy rainfalls. As we discussed above, flat topography limits the TOPMODEL-based approach and high-intensity rainfalls lead to more surface water. In other words, the $I_{VIC + Topmodel}$ can probably degenerate into the scheme estimating inundation extent directly from the uniform water table scheme. In this case, the $I_{VIC + Topmodel}$ does not respond to surface water and has a poor performance in water table redistribution. The I_{new}, however, has the mechanism to capture surface water dynamic, and thus, it can still perform well in flat topography. According to the example in the Eastern China, the new scheme can produce 47.4% and 33.3% more in the inundation extent and methane emissions, respectively. Because western Europe does not have the similar long-term rainy season, the new scheme only estimates 38.2% and 30.4% more inundation extent and methane emissions, respectively; (3) in arid regions, inundated area is mainly caused by intense rainfalls and most of surface water is produced from the Horton runoff [*Horton*, 1933]. Moisture deficit can be large, and unsaturated zones may exist under overland flow in these regions. In comparison to moist soil, more surface water will lose in the reinfiltration process, and the I_{new} may overestimate inundation extent and also its duration. Moreover, our "always saturated" assumption may lead to an overestimation of methane production zone in arid regions. However, the low carbon substrate availability can reduce this overestimation to some extent. The example in Australia indicates that the new scheme yields 137.0% and 83.8% raise in the inundation extent and methane emissions, respectively.

5. Discussions

We are also aware of the limitations in our model:

1. The redistribution function (equation (1)) is highly dependent on the decay parameter m which is a function of soil temperature, surface slope, and soil texture. The values were assigned for each grid cell according to previous study rather than calibration, which may introduce biases in water table redistribution.
2. The hydrological model can largely influence the performance of methane model. The validation shows that the VIC model used in this study may overestimate the soil moisture in high-latitude regions and underestimate that in trophic regions.
3. The description of methane production, oxidation, and transportation processes may have inherent uncertainties. For example, NPP is used as the proxy for the availability of organic carbon substrate in our model. However, the vegetation in the arctic regions usually has low carbon uptake ability and high carbon storage due to the low decomposition rate. In this case, our model can be potentially improved by using soil organic carbon directly.
4. Wetland is simply defined as inundated areas, but wetland-specific vegetation types (e.g., boreal peatlands, marsh, and mangroves) are not explicitly modeled. Our model can be further improved with consideration of more detailed microtopograhical variations such as hollows or hummocks in peatlands.
5. Seasonal change of vegetation cover may have large effect on controlling precipitation arriving at ground surface and flow velocity. In this study, their influences are partially considered by using seasonal leaf area index in the VIC model simulation. However, the manning's coefficient describing surface roughness is assumed constant (0.1). We will improve our future work in this area by cooperation with the developers of the CaMa-Flood model.

Moreover, the loss of surface water in evaporation or reinfiltration was not considered in our model. Although surface runoff may be not enough to fill unsaturated zones along its pathway in arid and dry regions, its low soil organic carbon may reduce possible errors in methane emissions. The assumption of always saturated soil column under inundated area may be not true especially for short time applications, while the simulation at the daily time step in this study can reduce the potential bias. Moreover, the detailed modeling of reinfiltration process usually requires a short time step (second or minute) which limit its applications at a large scale. For better validation of inundation extent, remote sensing technologies, which can provide large-scale inundated area at frequent temporal resolutions, is needed. The sensors, which are insensitive to dense canopy and clouds, are particularly useful in monitoring inundated area. The site-level calibration of methane models is important to reduce uncertainties in parameters [*Zhu et al.*, 2014], and more measurements of long-term methane fluxes are required. However, the scale issue associated with site-level data is still an open question. The methane concentration observations from satellites provide a good way to validate large-scale methane emissions [*Miller et al.*, 2013]. More data of accurate a priori methane source are required to reduce errors in converting measured concentrations to emissions estimations. At the same time, more efforts are needed to reduce uncertainties in inverse models [*Locatelli et al.*, 2013; *Miller et al.*, 2013].

6. Conclusions

The recent two methane model intercomparison projects in the global and region scales [*Melton et al.*, 2013; *Bohn et al.*, 2015] showed that existing schemes in estimating inundation extent lack the ability to capture flooded area due to horizontal movement of surface water. This limitation leads to an underestimation of inundation extent and thus tends to underestimate methane emissions. Our study found that the methane emissions model without surface routing module leads to 24.7% and 30.8% lower in estimating inundation extent and methane emissions at the global scale. The largest difference between the TOPMODEL-based approach and our proposed model in this study occurs in flat and moist regions, such as the Eastern China where the new methane model estimates 47.4% and 33.3% larger of the inundation extent and methane emissions than our previous methane model does. It was found that the impacts of surface water on the inundation extent and methane emissions vary with climate and topography: (1) compared to the current widely used TOPMODEL-based approach, the maximum inundation extent is larger from the proposed approach in this study almost for the whole global except for the high-latitude regions where snow melt mainly determines the inundated area; (2) the largest difference of estimated methane emissions between the two schemes occurs in flat regions with high precipitation.

In the light of wide recognition on the effects of methane emissions on climate change, accurate quantification of methane emissions is imperative for climate mitigation, and thus, improvement in methane emission models with consideration of critical processes such as surface water transport is indispensable. The scheme of coupling surface routing in this study only requires additional information of surface runoff without modifying model structure; thus, it will be applicable in most of the current methane models. Moreover, the surface routing method used in this study is publicly available, and the elevation-derived input data sets are also provided in the package. Here we provide an optional way for the community to analyze the effect of surface water transport on methane emissions. Finally, other than highlighting the significant effects of surface water transport on inundated area and methane emissions to the model community—lack of this component in methane model may lead to large bias—we stress that the estimates from our improved model can be used to better inform climate mitigation policies.

References

Avis, C., A. J. Weaver, and K. J. Meissner (2011), Reduction in areal extent of high-latitude wetlands in response to permafrost thaw, *Nat. Geosci.*, 4, 444–448, doi:10.1038/ngeo1160.
Beven, K. J., and M. J. Kirkby (1979), A physically based, variable contributing area model of basin hydrology, *Hydrol. Sci. Bull.*, 24, 43–69, doi:10.1080/02626667909491834.
Blazkova, S., K. Beven, P. Tacheci, and A. Kulasova (2002), Testing the distributed water table predictions of TOPMODEL (allowing for uncertainty in model calibration): The death of TOPMODEL?, *Water Resour. Res.*, 38(11), 1257, doi:10.1029/2001WR000912.
Bloom, A. A., P. I. Palmer, A. Fraser, D. S. Reay, and C. Frankenburg (2010), Large-scale controls of methanogenesis inferred from methane and gravity spaceborne data, *Science*, 327, 322–325, doi:10.1126/science.1175176.
Bohn, T. J., D. P. Lettenmaier, K. Sathulur, L. C. Bowling, E. Podest, K. C. McDonald, and T. Friborg (2007), Methane emissions from western Siberian wetlands: Heterogeneity and sensitivity to climate change, *Environ. Res. Lett.*, 2, 045015, doi:10.1088/1748-9326/2/4/045015.

Bohn, T. J., et al. (2015), WETCHIMP-WSL: Intercomparison of wetland methane emissions models over West Siberia, *Biogeosci. Discuss.*, *12*, 1907–1973, doi:10.5194/bgd-12-1907-2015.

Bousquet, P., et al. (2006), Contribution of anthropogenic and natural sources to atmospheric methane variability, *Nature*, *443*, 439–443, doi:10.1038/nature05132.

Bousquet, P., et al. (2011), Source attribution of the changes in atmospheric methane for 2006–2008, *Atmos. Chem. Phys.*, *11*, 3689–3700, doi:10.5194/acp-11-3689-2011.

Carter, A. J., and R. J. Scholes (2000), SoilData v2.0: Generating a global database of soil properties, Counc. for Sci. and Ind. Res. Environ., Pretoria, South Africa.

Denman, K. L., et al. (2007), Couplings between changes in the climate system and biogeochemistry, in *Climate Change 2007: The Physical Science Basis, Contribution of Working Group I to the Fourth Assessment Report of the Intergovernmental Panel on Climate Change*, edited by S. Solomon et al., chap. 7, pp. 1–90, Cambridge Univ. Press, Cambridge, U. K., and New York.

Dunne, T., and R. D. Black (1970a), An experimental investigation of runoff production in permeable soils, *Water Resour. Res.*, *6*(2), 478–490, doi:10.1029/WR006i002p00478.

Dunne, T., and R. D. Black (1970b), Partial area contributions to storm runoff in a small New England watershed, *Water Resour. Res.*, *6*(5), 1296–1311, doi:10.1029/WR006i005p01296.

Dunne, T., W. Zhang, and B. F. Aubry (1991), Effects of rainfall, vegetation, and microtopography on infiltration and runoff, *Water Resour. Res.*, *27*(9), 2271–2285, doi:10.1029/91WR01585.

Eliseev, A. V., I. I. Mokhov, M. M. Arzhanov, P. F. Demchenko, and S. N. Denisov (2008), Interaction of the methane cycle and processes in wetland ecosystems in a climate model of intermediate complexity, *Izv. Atmos. Ocean. Phys.*, *44*, 139–152, doi:10.1134/S0001433808020011.

Glagolev, M., I. Kleptsova, I. Flilippov, S. Maksyutov, and T. Machida (2011), Regional methane emission from West Siberia mire landscapes, *Environ. Res. Lett.*, *6*, 045214, doi:10.1088/1748-9326/6/4/045214.

Hansen, M. C., R. S. DeFries, J. R. G. Townshend, and R. Sohlberg (2000), Global land cover classification at 1 km spatial resolution using a classification tree approach, *Int. J. Remote Sens.*, *21*, 1331–1364.

Harriss, R., S. Wofsy, M. J. Hoell, R. Bendura, J. Drewry, R. J. Mc-Neal, D. Pierce, V. Rabine, and R. L. Snell (1994), The Arctic Boundary Layer Expedition (ABLE-3B): July–August 1990, *J. Geophys. Res.*, *99*, 1635–1643, doi:10.1029/93JD01788.

Hodson, E. L., B. Poulter, N. E. Zimmermann, C. Prigent, and J. O. Kaplan (2011), The El Niño–Southern Oscillation and wetland methane interannual variability, *Geophys. Res. Lett.*, *38*, L08810, doi:10.1029/2011GL046861.

Hopcroft, P. O., P. J. Valdes, and D. J. Beerling (2011), Simulating idealized Dansgaard-Oeschger events and their potential impacts on the global methane cycle, *Quat. Sci. Rev.*, *30*, 3258–3268, doi:10.1016/j.quascirev.2011.08.012.

Horton, R. E. (1933), The role of infiltration in the hydrologic cycle, *Eos Trans. AGU*, *14*(1), 446–460, doi:10.1029/TR014i001p00446.

Kalnay, E., et al. (1996), The NCEP/NCAR 40-year reanalysis project, *Bull. Am. Meteorol. Soc.*, *77*, 437–471.

Kaplan, J. O. (2002), Wetlands at the Last Glacial Maximum: Distribution and methane emissions, *Geophys. Res. Lett.*, *29*(6), 1079, doi:10.1029/2001GL013366.

Kim, H., P. J.-F. Yeh, T. Oki, and S. Kanae (2009), Role of rivers in the seasonal variations of terrestrial water storage over global basins, *Geophys. Res. Lett.*, *36*, L17402, doi:10.1029/2009GL039006.

Liang, X., D. P. Lettenmaier, E. F. Wood, and S. J. Burges (1994), A simple hydrologically based model of land surface water and energy fluxes for GSMs, *J. Geophys. Res.*, *99*, 14,415–14,428, doi:10.1029/94JD00483.

Locatelli, R., et al. (2013), Impact of transport model errors on the global and regional methane emissions estimated by inverse modelling, *Atmos. Chem. Phys.*, *13*, 9917–9937, doi:10.5194/acp-13-9917-2013.

Lu, X., and Q. Zhuang (2012), Modeling methane emissions from the Alaskan Yukon River basin, 1986–2005, by coupling a large-scale hydrological model and a process-based methane model, *J. Geophys. Res.*, *117*, G02010, doi:10.1029/2011JG001843.

Matthews, E., and I. Fung (1987), Methane emissions from natural wetlands: Global distribution, area, and environmental characteristics of sources, *Global Biogeochem. Cycles*, *1*, 61–86, doi:10.1029/GB001i001p00061.

Melillo, J. M., A. D. McGuire, D. W. Kicklighter, B. Moore III, C. J. Vörösmarty, and A. L. Schloss (1993), Global climate change and terrestrial net primary production, *Nature*, *363*, 234–240, doi:10.1038/363234a0.

Melton, J. R., et al. (2013), Present state of global wetland extent and wetland methane modelling: Conclusions from a model intercomparison project (WETCHIMP), *Biogeosciences*, *10*, 753–788, doi:10.5194/bg-10-753-2013.

Miller, S. M., et al. (2013), Anthropogenic emissions of methane in the United States, *Proc. Natl. Acad. Sci. USA.*, *110*(50), 20,018–20,022, doi:10.1073/pnas.1314392110.

Nguyen, P., A. Thorstensen, S. Sorooshian, K. Hsu, and K. AghaKouchak (2015), Flood forecasting and inundation mapping using HiResFlood-UCI and near real-time satellite precipitation data: The 2008 Iowa flood, *J. Hydrometeorol.*, *16*(3), 1171–1183, doi:10.1175/JHM-D-14-0212.1.

Nijssen, B., R. Schnur, and D. P. Lettenmaier (2001), Global retrospective estimation of soil moisture using the variable infiltration capacity land surface model, 1980–93, *J. Clim.*, *14*, 1790–1808, doi:10.1175/1520-0442(2001)014<1790:GREOSM>2.0.CO;2.

Norouzi, H., M. Temimi, A. AghaKouchak, M. Azarderakhsh, R. Khanbilvardi, G. Shields, and K. Tesfagiorgis (2015), Inferring land surface parameters from the diurnal variability of microwave and infrared temperatures, *Phys. Chem. Earth*, doi:10.1016/j.pce.2015.01.007.

Papa, F., C. Prigent, F. Aires, C. Jimenez, W. B. Rossow, and E. Matthews (2010), Interannual variability of surface water extent at the global scale, 1993–2004, *J. Geophys. Res.*, *115*, D12111, doi:10.1029/2009JD012674.

Pickett-Heaps, C. A., D. J. Jacob, K. J. Wecht, E. A. Kort, S. C. Wofsy, G. S. Diskin, D. E. J. Worthy, J. O. Kaplan, I. Bey, and J. Drevet (2011), Magnitude and seasonality of wetland methane emissions from the Hudson Bay Lowlands (Canada), *Atmos. Chem. Phys.*, *11*, 3773–3779, doi:10.5194/acp-11-3773-2011.

Pike, R. G. (1998), Current limitations of hydrologic modeling in BC: An examination of the HSPF, TOPMODEL, UBCWM and DHSVM hydrologic simulation models, BC Data Resources and Hydrologic-Wildfire Impact Modeling, Doctoral dissertation, Univ. of Victoria.

Prigent, C., F. Papa, F. Aires, W. B. Rossow, and E. Matthews (2007), Global inundation dynamics inferred from multiple satellite observations, 1993–2000, *J. Geophys. Res.*, *112*, D12107, doi:10.1029/2006JD007847.

Prigent, C., F. Papa, F. Aires, C. Jimenez, W. B. Rossow, and E. Matthews (2012), Changes in land surface water dynamics since the 1990s and relation to population pressure, *Geophys. Res. Lett.*, *39*, L08403, doi:10.1029/2012GL051276.

Riley, W. J., Z. M. Subin, D. M. Lawrence, S. C. Swenson, M. S. Torn, L. Meng, N. M. Mahowald, and P. Hess (2011), Barriers to predicting changes in global terrestrial methane fluxes: Analyses using CLM4Me, a methane biogeochemistry model integrated in CESM, *Biogeosciences*, *8*, 1925–1953, doi:10.5194/bg-8-1925-2011.

Ringeval, B., P. Friedlingstein, C. Koven, P. Ciais, N. de Noblet-Ducoudra, B. Decharme, and P. Cadule (2011), Climate-CH4 feedback from wetlands and its interaction with the climate-CO2 feedback, *Biogeosciences*, *8*, 2137–2157, doi:10.5194/bg-8-2137-2011.

Ringeval, B., et al. (2012), Modelling subgrid wetland in the ORCHIDEE global land surface model: Evaluation against river discharges and remotely sensed data, *Geosci. Model Dev.*, *5*, 683–735, doi:10.5194/gmdd-5-683-201210.5194/gmdd-5-683-2012.

Rofaier, A. M., A. Bartsch, and W. G. Rees (2013), Assessment of spring floods and surface water extent over the Yamalo-Nenets Autonomous District, *Environ. Res. Lett.*, *8*, doi:10.1088/1748-9326/8/4/045026.

Roulet, N., A. Jano, C. Kelly, and L. Klinger (1994), Role of the Hudson Bay Lowland as a source of atmospheric methane, *J. Geophys. Res.*, *99*, 1439–1454, doi:10.1029/93JD00261.

Schroeder, R., M. A. Rawlins, K. C. McDonald, E. Podest, R. Zimmermann, and M. Kueppers (2010), Satellite microwave remote sensing of North Eurasian inundation dynamics: Development of coarse-resolution products and comparison with high-resolution synthetic aperture radar data, *Environ. Res. Lett.*, *5*, 015003, doi:10.1088/1748-9326/5/1/015003.

Schroeder, R., K. C. McDonald, B. D. Chapman, K. Jensen, E. Podest, Z. D. Tessler, T. J. Bohn, and R. Zimmermann (2015), Development and Evaluation of a Multi-Year Fractional Surface Water Data Set Derived from Active/Passive Microwave Remote Sensing Data, *Remote Sens.*, *7*, 16,688–16,732, doi:10.3390/rs71215843.

Singarayer, J. S., P. J. Valdes, P. Friedlingstein, S. Nelson, and D. J. Beerling (2011), Late Holocene methane rise caused by orbitally controlled increase in tropical sources, *Nature*, *470*, 82–85, doi:10.1038/nature09739.

Spahni, R., et al. (2011), Constraining global methane emissions and uptake by ecosystems, *Biogeosciences*, *8*, 1643–1665, doi:10.5194/bg-8-1643-2011.

Tian, H., X. Xu, C. Lu, M. Liu, W. Ren, G. Chen, J. M. Melillo, and J. Liu (2011), Net exchanges of CO_2, CH_4, and N_2O between China's terrestrial ecosystems and the atmosphere and their contributions to global climate warming, *J. Geophys. Res.*, *116*, G02011, doi:10.1029/2010JG001393.

van Bodegom, P., J. Goudriaan, and P. Leffelaar (2001), A mechanistic model on methane oxidation in a rice rhizosphere, *Biogeochemistry*, *55*, 145–177.

Walter, B. P., and M. Heimann (2000), A process-based, climate-sensitive model to derive methane emissions from natural wetlands: Application to five wetland sites, sensitivity to model parameters, and climate, *Global Biogeochem. Cycles*, *14*, 745–765, doi:10.1029/1999GB001204.

Wania, R., I. Ross, and I. C. Prentice (2009), Integrating peatlands and permafrost into a dynamic global vegetation model. I: Evaluation and sensitivity of physical land surface processes, *Global Biogeochem. Cycles*, *23*, GB3014, doi:10.1029/2008GB003412.

Wania, R., I. Ross, and I. C. Prentice (2010), Implementation and evaluation of a new methane model within a dynamic global vegetation model: LPJ-WHyMe v1.3.1, *Geosci. Model Dev.*, *3*, 565–584, doi:10.5194/gmd-3-565-2010.

Wania, R., et al. (2013), Present state of global wetland extent and wetland methane modelling: Methodology of a model intercomparison project (WETCHIMP), *Geosci. Model Dev.*, *6*, 617–641, doi:10.5194/gmd-6-617-2013.

Winderlich, J., H. Chen, C. Gerbig, T. Seifert, O. Kolle, J. V. Lavrič, C. Kaiser, A. Höfer, and M. Heimann (2010), Continuous low-maintenance CO2/CH4/H2O measurements at the Zotino Tall Tower Observatory (ZOTTO) in Central Siberia, *Atmos. Meas. Tech.*, *3*, 1113–1128, doi:10.5194/amt-3-1113-2010.

Worthy, D. E. J., I. Levin, F. Hopper, M. K. Ernst, and N. B. A. Trivett (2000), Evidence for a link between climate and northern wetland methane emissions, *J. Geophys. Res.*, *105*, 4031–4038, doi:10.1029/1999JD901100.

Wu, H., R. F. Adler, Y. Tian, G. J. Huffman, H. Li, and J. Wang (2014), Real-time global flood estimation using satellite-based precipitation and a coupled land surface and routing model, *Water Resour. Res.*, *50*, 2693–2717, doi:10.1002/2013WR014710.

Xu, X., and H. Tian (2012), Methane exchange between marshland and the atmosphere over China during 1949–2008, *Global Biogeochem. Cycles*, *26*, GB2006, doi:10.1029/2010GB003946.

Yamazaki, D., S. Kanae, H. Kim, and T. Oki (2011), A physically based description of floodplain inundation dynamics in a global river routing model, *Water Resour. Res.*, *47*, W04501, doi:10.1029/2010WR009726.

Yamazaki, D., H. Lee, D. E. Alsdorf, E. Dutra, H. Kim, S. Kanae, and T. Oki (2012a), Analysis of the water level dynamics simulated by a global river model: A case study in the Amazon River, *Water Resour. Res.*, *48*, W09508, doi:10.1029/2012WR011869.

Yamazaki, D., C. Baugh, P. D. Bates, S. Kanae, D. E. Alsdorf, and T. Oki (2012b), Adjustment of a spaceborne DEM for use in floodplain hydrodynamic modelling, *J. Hydrol.*, *436/437*, 81–91, doi:10.1016/j.jhydrol.2012.02.045.

Zakharova, E. A., A. V. Kouraev, S. Biancamaria, M. V. Kolmakova, N. M. Mognard, V. A. Zemtsov, S. N. Kirpotin, and B. Decharme (2011), Snow cover and spring flood flow in the Northern Part of Western Siberia (the Poluy, Nadym, Pur, and Taz Rivers), *J. Hydrometeorol.*, *12*(6), 1498–1511, doi:10.1175/JHM-D-11-017.1.

Zhu, X., Q. Zhuang, X. Lu, and L. Song (2014), Spatial scale-dependent land–atmospheric methane exchanges in the northern high latitudes from 1993 to 2004, *Biogeosciences*, *11*, 1693–1704, doi:10.5194/bg-11-1693-2014.

Zhuang, Q., V. E. Romanovsky, and A. D. McGuire (2001), Incorporation of a permafrost model into a large-scale ecosystem model: Evaluation of temporal and spatial scaling issues in simulating soil thermal dynamics, *J. Geophys. Res.*, *106*(D24), 33,649–33,670, doi:10.1029/2001JD900151.

Zhuang, Q., et al. (2003), Carbon cycling in extratropical terrestrial ecosystems of the Northern Hemisphere during the 20th century: A modeling analysis of the influences of soil thermal dynamics, *Tellus Ser. B.*, *55*, 751–776.

Zhuang, Q., J. M. Melillo, D. W. Kicklighter, R. G. Prinn, A. D. McGuire, P. A. Steudler, B. S. Felzer, and S. Hu (2004), Methane fluxes between terrestrial ecosystems and the atmosphere at northern high latitudes during the past century: A retrospective analysis with a process-based biogeochemistry model, *Global Biogeochem. Cycles*, *18*, GB3010, doi:10.1029/2004GB002239.

Zhuang, Q., J. M. Melillo, D. W. Kicklighter, R. G. Prinn, A. D. McGuire, B. S. Felzer, A. Sokolov, R. G. Prinn, P. A. Steudler, and S. Hu (2006), CO_2 and CH_4 exchanges between land ecosystems and the atmosphere in northern high latitudes over the 21st century, *Geophys. Res. Lett.*, *33*, L17403, doi:10.1029/2006GL026972.